

Radar imaging of fractures and voids behind the walls of an underground mine

Amin Abbasi Baghbadorani¹, John A. Hole¹, Jonathan Baggett², and Nino Ripepi³

ABSTRACT

Two- and three-dimensional rock-penetrating-radar data were acquired on the wall of a pillar in an underground limestone mine. The objective was to test the ability of radar to image fractures and karst voids and to characterize their geometry, aperture, and fluid content, with the goal of mitigating mining hazards. Strong radar reflections in the field data correlate with fractures and a cave exposed on the pillar walls. Large pillar wall topography was included in the steep-dip Kirchhoff migration algorithm because standard elevation corrections are inaccurate. The depth-migrated 250 MHz radar images illuminate fractures, karst voids, and the far wall of the pillar up to approximately 25 m depth into the rock, with a spatial resolution of < 0.5 m. Higher frequency radar improved the image resolution and aided in the interpretation, but at the cost of shallower depth of penetration and extra acquisition effort. Due to the strong contrast in physical properties between the rock and the fracture fluid, fractures with apertures as thin as a 50th of a radar wavelength were imaged. Water-filled fractures with mm-scale aperture and air-filled fractures with cm-scale apertures produce strong reflections at 250 MHz. A strong variation in the reflection amplitude along each fracture is interpreted to represent the variable fracture aperture and the nonplanar fracture structure. Fracture apertures were quantitatively measured, but distinguishing water from air-filled fractures was not possible due to the complex radar wavelet and fracture geometry. Two conjugate fracture sets were imaged. One of these fracture sets dominates the rock mass stability and water inrush challenges throughout the mine. All of the detected voids and a large cave are at the intersection of two fractures, indicating preferential water flow and dissolution along conjugate fracture intersections. Detecting, locating, and characterizing fractures and voids prior to excavation can enable miners to mitigate potential collapse and flood hazards before they occur.

INTRODUCTION

Undetected fractures and voids can pose structural collapse (ground control) hazards and flood (water inrush) hazards during mining and other excavation. Underground mining has one of the highest fatal injury rates of any U.S. industry, more than five times the national average compared with other industries (CDC, 2019a). Between 1999 and 2008, almost 40% of all underground fatalities were attributed to roof, rib, or face collapse. Many injuries and fatalities are related to weak geologic structures, such as thinly bedded rock, clay, discontinuities, paleochannels, faults, or fractures (CDC, 2019b).

Such incidents are not unique to the United States and affect mining, tunneling, and other excavation operations globally. A second major hazard is flooding due to excavation into old mines, highly permeable rock, or open fractures. For instance, in China, 496 major water inrush accidents from 2001 to 2015 resulted in 3255 deaths (Qi et al., 2017). Even without injuries, remediation of unanticipated collapse and water inrush is a major cost to mining operations.

Fractures and voids are a fundamental mechanical weakness and the main water inrush pathway in bedrock. Probe drilling is the primary method of detecting these hazards prior to excavation (e.g., Li et al., 2010; Liu et al., 2017), but they often remain undetected until after blasting. Fractures and voids can have complex geometries and

Manuscript received by the Editor 13 October 2020; revised manuscript received 15 April 2021; published ahead of production 19 May 2021; published online 12 July 2021.

Virginia Tech, Department of Geosciences, Blacksburg, Virginia 24061, USA. E-mail: amin4@vt.edu (corresponding author); hole@vt.edu. ²Formerly Virginia Tech, Department of Mining and Minerals Engineering, Blacksburg, Virginia 24061, USA; presently Rio Tinto Copper, Kennecott Underground Copper, Salt Lake City, South Jordan, UT 84009, USA. E-mail: jonb4@vt.edu.

Virginia Tech, Department of Mining and Minerals Engineering, Blacksburg, Virginia 24061, USA. E-mail: nripepi@vt.edu. © 2021 Society of Exploration Geophysicists. All rights reserved.

highly variable apertures so that a hazardous zone can lie between or beyond drillholes and be absent or subtle where drilled.

Limestone is widely excavated globally from open quarries and underground mines for crushed stone, building stone, and chemical lime (e.g., Bliss et al., 2008). It is a mechanically strong rock (e.g., Johnson and DeGraff, 1988). However, joints and fractures can form under stress or be caused by the removal of stress during exhumation, reducing the strength of the rock mass, and providing groundwater flow paths. The main mineral component of limestone is calcite (calcium carbonate), which is highly soluble in water at geologic time scales, so groundwater flow dissolves and enlarges the fractures. Limestone proximal to earth's surface typically forms a karst landscape and groundwater system consisting of open fractures and caves, which are mechanically weak and are fluid conduits capable of holding and transporting significant volumes of fluid (e.g., Dreybrodt, 1988). Therefore, fractures and open voids are a larger hazard in limestone mining than in other types of mining. However, fracture hazards and this radar work are highly relevant to other rock settings as well as other types of excavations such as tunneling.

Ground-penetrating radar (GPR) is a versatile and nonintrusive geophysical tool that has been used to image earth's shallow subsurface and engineered materials for many applications (e.g., Jol, 2009). In electrically resistive bedrock, GPR penetration can be many tens of radar wavelengths, much deeper than can usually be imaged in more electrically conductive soil or sediment (e.g., Jol, 2009). This deeper penetration usually requires GPR data acquisition directly on exposed rock surfaces.

Several studies have addressed the detection of fractures and voids in rock in underground mines (e.g., Annan et al., 1988; Derobert and Abraham, 2000; Grodner, 2001; Kovin, 2011), quarries (e.g., Grasmueck, 1996; Toshioka et al., 1995; Grandjean and Gourry, 1996; Orlando, 2003; Grasmueck et al., 2004; Porsani et al., 2006; Markovaara-Koivisto et al., 2014), road cuts (e.g., Pipan et al., 2003; Longoni et al., 2012), unstable rock slopes (e.g., Heincke et al., 2005; Jeannin et al., 2006; Theune et al., 2006), tunnels (e.g., Apel and Dezelic, 2005a; Prego et al., 2016), and hazardous waste disposal sites (e.g., Stevens et al., 1995; Baek et al., 2017). Fractures in limestone have been imaged by GPR from surface or quarry outcrops (e.g., Orlando, 2003; Pipan et al., 2003; Grasmueck et al., 2004; Apel and Dezelic, 2005b; Jeannin et al., 2006; Longoni et al., 2012). Fractures have also been imaged to assess the strength of a pillar in an underground gypsum mine (Dérobert and Abraham, 2000). This study images fractures in limestone in an underground

The aperture, or wall-to-wall thickness, of the fractures imaged in most of the above studies is less than a quarter wavelength of the radar waves. Thus, the fractures are thin layers, in which the waves reflected from the two walls of the fracture destructively interfere and decrease the reflected signal amplitude. However, the very strong contrast in relative dielectric permittivity (dielectric constant) and radar wavespeed between the rock and fluids (air or water) enables detectable radar reflections from very thin fractures (e.g., Grasmueck, 1996; Kallweit and Wood, 1982; Toshioka et al., 1995; Lane et al., 2000; Apel and Dezelic, 2005b; Leucci et al., 2007; Kovin, 2011). In principle, the amplitude and phase of the reflected waveforms can be used to distinguish air, water, or fine-grained loose rock particles filling the fractures (e.g., Grégoire and Hollender, 2004; Deparis and Garambois, 2009; Markovaara-Koivisto et al., 2014; Arosio, 2016; Baek et al., 2017). This has usually proven difficult with realistic field data. Fractures and voids are complex 3D structures. Three-dimensional radar imaging has shown to be effective at delineating complex subsurface structures (e.g., Grasmueck, 1996; Young et al., 1997; Gross et al., 2003; Grasmueck et al., 2004; McClymont et al., 2008; Christie et al., 2009; Liu et al., 2021), but the geometry of karst caves can be challenging.

Baggett et al. (2020) acquire GPR data on a vertical wall of a pillar in an underground limestone mine. The pillar was chosen because a karst cave and fractures are exposed on its walls. Similar features have caused collapse and water inrush throughout the study site mine during excavation and have been costly to mine operations. The GPR data were converted from time to depth using a constant velocity, and they were draped on the smoothed wall topography. This enabled correlation of the GPR reflections to fractures observed on the pillar walls and a discussion of applications to mining (Baggett et al., 2020). However, the reflectors were at steep angles relative to the data acquisition surface, the pillar wall. Migration is needed to properly locate the fractures.

This paper reports the results of working with the same GPR data as Baggett et al. (2020) but uses migration to image the fractures in two and three dimensions. In addition, the reflection amplitudes were calibrated to enable quantitative characterization of the fractures and voids. The primary goal was to develop more quantitative methods that could be used ahead of mining to model and mitigate these hazards before excavation. A secondary goal was to understand fracturing and karst processes at the mine.

THE LIMESTONE MINE

Data acquisition occurred in an underground, multilevel limestone mine. The mine is producing rock for chemical lime with few impurities such as silica (97%-98% calcium carbonate) (mine personnel, personal communication, 2018). The stratigraphic deposit is a dipping massive limestone unit bounded by limestone and dolomite with higher silica content (Figure 1a). Sedimentary diagenesis has recrystallized the original calcite and closed most of the original porosity. The stratigraphic ore body dips approximately 30°, and it is approximately 30m thick. The nominal tunneling design consists of two approximately 12 m wide, approximately 8 m tall tunnels at each level, separated by approximately 24 m wide square pillars and cross tunnels (Figure 1b). Mining extends downdip to approximately 0.3 km lower than the mine entrance and approximately 0.6 km vertically beneath the upward-sloping surface (Figure 1a).

The limestone ore and adjacent carbonate members contain numerous karst features. Fractures and voids have been encountered throughout the mine and range in size from nondisplaced fractures to caves with volumes of several hundred cubic meters. When mining production blasts and excavation breach open fractures or voids, rock blocks, fluid-suspended clay-sized rock particles (slurry), and water can enter into the mine tunnel, sometimes with very large volumes. Water is continuously being pumped from the mine. Continuous water inflow rates correlate within hours with surface rainfall and surface-stream flow. Chemical dye tests indicate groundwater flow speed >500 m/day.

THE PILLAR

The GPR survey was conducted on the vertical wall of a pillar that has a triangular prism shape with two walls approximately 40 m long and a wall approximately 25 m long (Figure 1c). The tunnels and pillar are approximately 10 m tall. The pillar is approximately 125 m lower than the mine entrance and approximately 250 m vertically below the surface. The primary reason to choose this pillar was the existence of fractures and a large cave within the pillar (Figures 1 and 2). Three fractures can be observed on the front wall (FW) of the pillar where the radar data were acquired (Figure 1). These fractures and additional fractures and a large cave on the far (south) wall of the pillar provide radar imaging targets. A lack of known fractures in the eastern half of the pillar provides a reference for comparison. This pillar was also chosen for its atypical triangular geometry so that potential radar reflectors inside the pillar are not parallel to potential reflections from the tunnel wall behind the radar operators.

The cave in the southern tunnel is up to approximately 5 m wide and extends at least 4 m into the pillar and into the other wall of the tunnel. It extends from near the tunnel floor to at least 5 m above the tunnel ceiling (Figures 1 and 2). The pillar was excavated to be triangular to create an easier truck passage from the north tunnel to the south tunnel beyond the cave, while the cave's hazards were being mitigated. The cave has since been secured with rock bolts, metal straps, and plastic mesh to prevent rocks from falling into the tunnel (Figure 2).

Fracture F1 (Figures 1 and 3) is the most obvious fracture in the northern, radar-acquisition tunnel, and it is visible on the tunnel walls and ceiling. Its orientation is consistent with it intersecting the cave on the far side of the pillar. This fracture is closed (the fracture walls are in contact) near the tunnel floor, but it is locally open with up to approximately 1 cm aperture near the top of the pillar wall. A V-shaped concavity in the tunnel wall at F1 (Figures 1 and 3) was caused by a rockfall from the side of the fracture during excavation. The eastern side of the V is the fracture surface. This surface and other fracture surfaces in the mine have visible mineral alteration.

Fractures F2 and F3 to the west of F1 (Figure 1) are less obvious, closed, and cannot be easily traced across the tunnel ceiling. The orientations of the F fractures are similar to each other and to known hazardous fractures throughout the mine, a fracture set created by local stress. There are multiple fractures on the southern wall of the pillar between the cave and the corner that may correlate to F2 and F3. All three F fractures range from wet to trickling water, depending on recent precipitation at the surface.

RADAR DATA ACQUISITION

The rock-penetrating radar data acquisition used Sensors & Software Inc. equipment with nominal center frequencies of 200, 250, 500, and 1000 MHz (Baggett et al., 2020). The data acquisition parameters are listed in Table 1. The 200 MHz system is unshielded, with physically separated transmitter and receiver antennae. This configuration allows for data acquisition techniques that can determine the radar wavespeed, or velocity, of the rock. The 250, 500, and 1000 MHz systems are shielded and are packaged in a fixedoffset configuration. The 200 MHz unshielded and 250 MHz shielded systems allow a comparison of the ability for shielded antennae to eliminate unwanted air-wave reflections from tunnel walls behind the operator. All data, except for the velocity survey, were acquired in the common-offset mode with a fixed transmitterreceiver offset (Table 1).

Lower frequency (200 and 250 MHz) 2D surveys were acquired in a horizontal survey line along the entire approximately 41 m length of the pillar's north wall (Figure 1). The curvature of this pillar wall is more than 30% of the line length, and local wall relief varies from a few centimeters to approximately 2 m. To eliminate signal loss by keeping the antennae in contact with the rock, data were collected by moving the antennae the desired distance and triggering acquisition manually. Stations were marked on a reflective ribbon nailed to the rock approximately 1 m above the tunnel floor. The ribbon was surveyed for location at approximately 6 m spacing by infrared transit, and radar stations were interpolated; this oc-

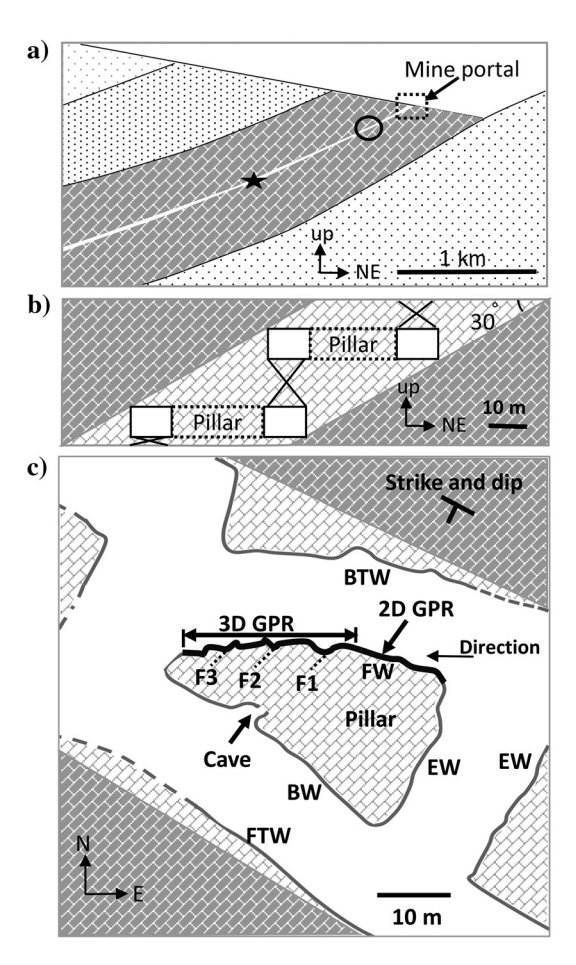


Figure 1. (a) Cross section through the mine. The lime ore unit (the white line) lies within a thicker limestone sequence. The circle indicates the level of this study, and the star is the deepest level of the mine. (b) Cross section showing two mine levels. White is the tunnels. The geology is limestone, but the darker units are not of ore quality. Cross-cut tunnels (dashed) connect the entry tunnels at each level, so that the pillars are nominally 23×23 m horizontal $\times 8$ m high. Crossed-out volumes between levels will be stope mined later. (c) Map view of the pillar used in this study, surveyed using LIDAR. The triangular shape is unusual; tunnels were deviated after mining into the cave. The thick black line represents the 200 and 250 MHz radar 2D survey line, and the double-arrow section is the 500 and 1000 MHz 2D and 250 MHz 3D surveys. The locations of fractures F1, F2, and F3 on the tunnel wall and their orientations are indicated. North is nominal in a local coordinate system.

curred prior to access to the LIDAR equipment described below. The antennae were oriented perpendicular to the survey line, vertical against the pillar wall. The number of radar pulses stacked (added) together (Table 1) is a compromise between data quality and acquisition time, decided during data acquisition based on the observed signals.

To measure the radar velocity in the limestone, data were acquired around a corner of the pillar that has no visible fractures. The 200 MHz transmitter was kept fixed on one wall of the pillar, and the receiver was moved along another wall in 10 cm increments (Figure 4). Although the transmitter location and the endpoints of the receiver line were accurately surveyed by infrared transit, interpolated station locations were imperfect due to the wall roughness and curvature.

Data acquisition with the higher frequency of 500 and 1000 MHz systems requires smaller station spacing (Table 1), which makes manual data collection more time-consuming and prone to user error. Therefore, data acquisition was automatically triggered using a wheeled odometer. However, the roughness of the pillar wall caused the wheel to skip and prevented the odometer from consistent triggering. Several 2.4 m long wood planks were attached to the pillar wall to create a smooth platform for the survey. The gap between the planks and pillar wall ranged from flush to a few radar wavelengths. The gap reduces the amount of signal penetrating the wall because a significant portion of the signal will reflect at the air-rock boundary (the reflection coefficient is determined below to be 0.44). The gap also reduces the effect of antenna shielding due to the reflected signal. The variability of the gap also creates a variable time delay,



Figure 2. Mitigated large cave in the southern tunnel of Figure 1. The tunnel wall on the left of the photo is the south wall (BW) of the pillar. From Baggett et al. (2020).

which damages wavefield coherence. The length of the higher frequency surveys was approximately 24 m, extending across fractures F1-F3 (Figure 1). The pillar wall and planks were surveyed for location by a 3D LIDAR laser scanner (for the LIDAR images, see Baggett et al., 2020), and station locations were interpolated along the straight planks.

A grid of 3D data was acquired using the 250 MHz system. An approximately 3×3 m tarp was painted with a grid of stations that was detectable with the LIDAR, and it was hung on the wall (Figure 3). Stations were accessed by a lift machine and manually triggered. This was an awkward operation due to lack of fine motor control on the lift. Seven vertical lines and six horizontal lines were acquired on the tarp with 0.5 m line spacing and 10 cm station spacing. The tarp was deployed eight times to survey a swath approximately 24 m long × approximately 3 m high. LIDAR was used to survey the pillar wall and the stations on each tarp (Figure 3b)



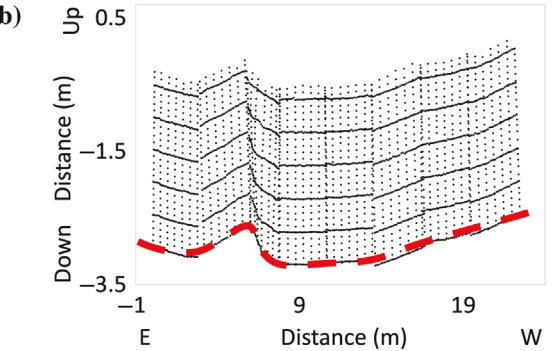


Figure 3. (a) The 3D radar data collection against a marked tarp hung on the pillar wall. Fracture F1 is just past the right side of the tarp. (b) 3D radar station coordinates. The vertical axis is exaggerated. The regular grid is distorted by wall roughness. The red line is approximately along the 2D profile.

Table 1. Radar systems and data acquisition parameters.

GPR model	Frequency (MHz)	Survey length (m)	Step size (m)	Antenna separation (m)	Time window (ns)	Time sampling interval (ps)	Number of stacked traces
PulseEKKO	200	39.6	0.1	0.5	750.8	400	32
Noggin	250	39.6	0.1	0.25	1100	400	64
	500	24.7	0.05	0.155	660	200	16
	1000	24.2	0.01	0.075	220.1	100	32

(Baggett et al, 2020). The tarps bridged the topography, but not as much as the planks because the tarp could be folded over bumps. The amount of bridging was a fraction of the 250 MHz radar wavelength.

RADAR PROPERTIES OF THE MINE MATERIALS

In this mine, the materials of interest are limestone, groundwater, clay-sized rock particles suspended in groundwater (slurry), and air. The radar wavespeed (velocity), wavelength, and attenuation depend on the electrical conductivity and relative dielectric permittivity (dielectric constant) of these nonmagnetic materials (e.g., Jol, 2009). The electrical conductivity of the mine water and slurry was measured in the laboratory by an Oakton CON 6+ conductivity meter and found to be similar to fresh water (Table 2). The low conductivity of the slurry indicates that the clay-sized particles are not dominated by conductive clay minerals. The electrical conductivity of limestone ranges from 10^{-2} to 10^{-5} S/m (Telford et al, 1990; Daniels, 2004). Because the limestone in the mine is > 97%carbonate with no clay content and very low porosity, a conductivity $\leq 10^{-3}$ S/m is expected. The dielectric constants of the materials were obtained from Telford et al. (1990) and Daniels (2004), and it was assumed that the slurry behaves like water (Table 2).

The radar velocity of the limestone pillar was derived from the transmission survey (Figure 4). The velocity was calculated to be 0.117 ± 0.002 m/ns by linear regression of the rock-wave arrival time versus the straight-line distance between the transmitter and the receiver. Because the massive limestone formation is quite homogeneous and no fractures were noticed in this corner of the pillar, this number is assumed to be representative of unfractured rock in the pillar. The velocity corresponds to a wavelength of 59-12 cm at radar frequencies of 200-1000 MHz, respectively (Table 2). The radar velocity in the water and the slurry is approximately 3.5 times slower, and the radar velocity in the air is approximately 2.5 times faster than the limestone, with corresponding differences in the wavelength (Table 2). These very large differences between the rock and fluid properties cause very strong reflection coefficients at the rock-fluid boundaries.

Attenuation of radar depends on the electrical conductivity. Lowloss materials (poor conductors) are those where $\sigma/\omega\varepsilon \ll 1$, where σ is the electrical conductivity in siemens/m of the material, ε is the dielectric permittivity in F/m, and ω is the angular frequency of the radar or 2π times the frequency (Daniels, 2004). All mine materials, even the moderately conductive water and slurry, have low loss at radar frequencies (Table 2). Using the full complex wavenumber equation (Daniels, 2004), the exponential damping constant was calculated to be 1-2 m in the water and slurry and approximately 15 m in the limestone (Table 2). This corresponds to the one-way distance in which the wave attenuates to 1/e or approximately 37% in amplitude.

PRELIMINARY PROCESSING AND INTERPRETATION

Preprocessing was applied to the data in the field for quality control and then more carefully applied in the laboratory. A mix of proprietary radar and seismic reflection processing software was used: Ekko Project (Sensors and Software, 2018), SeisSpace (Halliburton, 2020), and DUG Insight (DownUnder GeoSolutions, 2020). Data at all frequencies were treated in a similar manner. The 2D or 3D station geometry was assigned to each radar trace based on the infrared transit (200 and 250 MHz 2D data) or LIDAR (500 and 1000 MHz 2D data and 250 MHz 3D data). Most geophysics software is written for data acquired on earth's surface and imaging downward; therefore, a local Cartesian x, y, and z were assigned to east, up, and south, respectively; the software's "down" is south into our pillar.

The trace recording start time was adjusted based on the observed direct wave. Most GPR systems generate a radar pulse with a bandwidth centered near its nominal frequency f_0 (Table 1). The data were band-pass filtered from $f_0/2$ to $2f_0$. The high-cut frequency avoided aliasing at the station spacing (Table 1). For the 3D data, a

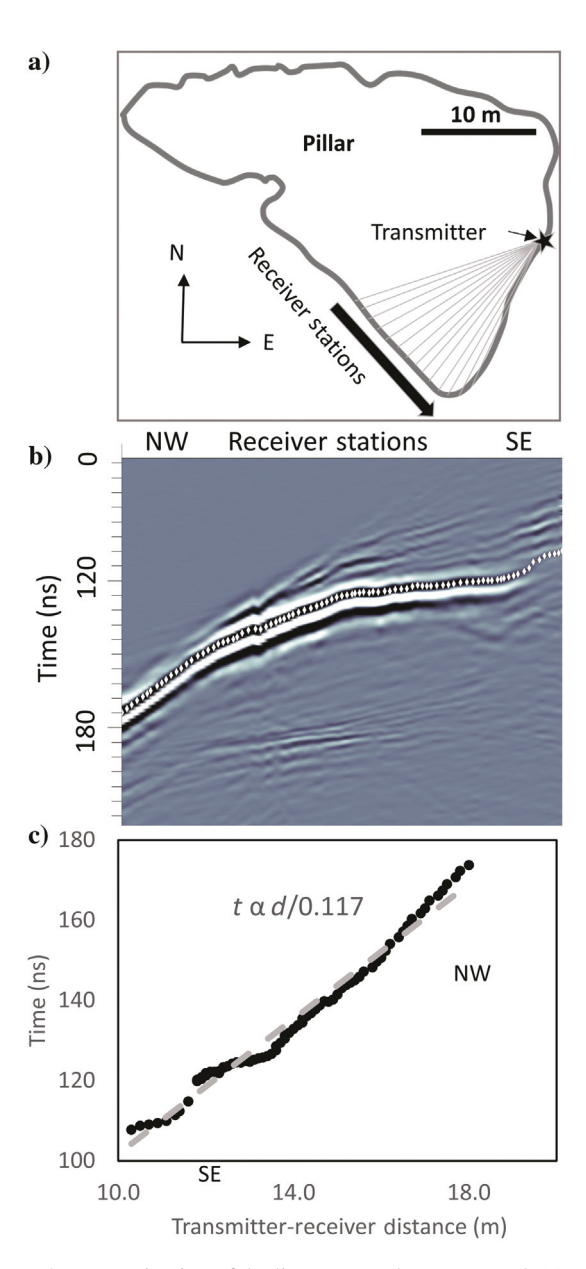


Figure 4. Determination of the limestone radar wavespeed. (a) Map of the radar transmission data acquisition geometry and raypaths in a corner of the pillar without fractures. (b) Radar 200 MHz data, with symbols indicating the direct rock arrival. (c) Linear fit of the transmitted traveltime versus the straight-line distance.

lower high-cut frequency of $1.5f_0 = 375$ MHz was used to reduce 3D spatial aliasing caused by the larger 0.5 m spacing between lines. The data were corrected for amplitude loss due to spherical divergence. The amplitude of each sample on each trace was multiplied by time, which is proportional to distance in the constantvelocity limestone.

Air-wave reflections from objects in the air behind or beside the operator can clutter GPR data. In this case, the mine tunnel wall approximately 13 m behind the GPR operator is in the optimum geometry to produce a reflection. The 200 MHz unshielded and 250 MHz shielded systems enable a comparison of these effects. Because the two systems have different transmitter power and fre-

quency bandwidth, a constant gain and proportional frequency filter was applied to roughly equalize the amplitudes and bandwidth (but not the frequency) of features in the data that are interpreted to be from radar waves that traveled within the pillar. A roughly horizontal reflection from the wall behind the operator, labeled behind tunnel wall (BTW) in Figure 5 is observed at 85-105 ns in the unshielded antenna data, and this event is much weaker or absent in the data from the shielded antenna, illustrating the value of shielding. However, the shielding does not completely eliminate the unwanted air wave. This may be in part due to the antennae not always being flush against the wall due to wall roughness. The unshielded 200 MHz GPR system has much greater power; therefore, deeper events in these data had a better signal-to-noise ratio (not shown). However, the signal-to-noise was sufficient in the 250 MHz data, and due to the weaker air-wave reflections, these data were used for subsequent interpretation.

Figure 6 shows the 250 MHz radar data after spherical divergence correction as described above. The known pillar and tunnel geometry enable calibrated interpretation of many of the observed events in these data. Images similar to this but with nonoptimized parameter choices were available in the field, which enabled real-time calibration and detection of the larger amplitude events.

The southern back wall of the pillar produces a strong reflection, labeled back wall (BW) in Figure 6. This reflector extends from near-zero time near the western corner of the pillar to 425 ns

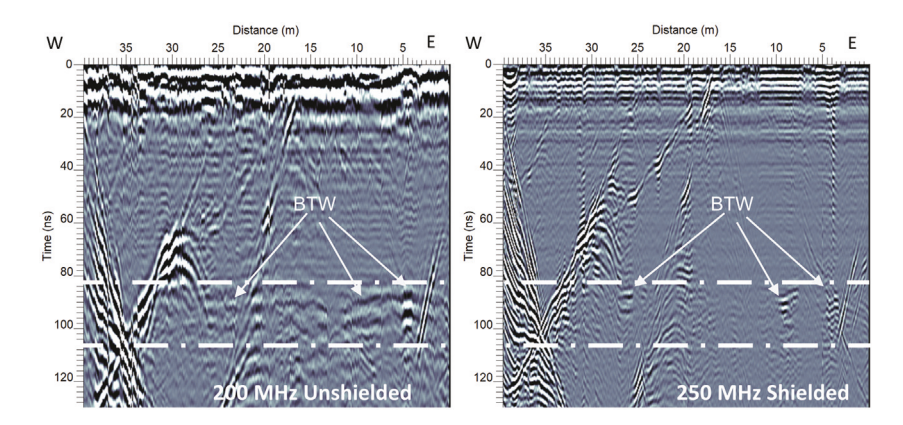


Figure 5. Radar data for the 200 MHz unshielded antennae and 250 MHz shielded antennae. Plots are scaled so that the steep events on the left half of both figures have approximately equal amplitude. BTW indicates reflections from the tunnel wall behind the operator, which are stronger in the unshielded data.

Table 2. Electrical properties of the materials encountered in the mine.

Electrical property	Frequency f (MHz)	Air	Limestone	Slurry	Water
Velocity (m/ns)	All	0.3	0.117	0.033	0.033
Wavelength (m)	200	1.50	0.585	0.165	0.165
	250	1.20	0.468	0.132	0.132
	500	0.60	0.234	0.066	0.066
	1000	0.30	0.117	0.033	0.033
Fresnel zone at 10 m (m)	200	2.74	1.71	0.91	0.91
	250	2.45	1.53	0.81	0.81
	500	1.73	1.08	0.57	0.57
	1000	1.22	0.76	0.41	0.41
Electrical conductivity ⁴ σ (S/m)	All	0	≤0.001	0.0259	0.0371
Dielectric constant ⁵ $\varepsilon_{\rm r}$	All	1	8	81	81
$\sigma/(2\pi f \varepsilon_0 \varepsilon_{\rm r}) = \sigma/(\omega \varepsilon)$	200	0.0000	0.0112	0.0287	0.0412
	250	0.0000	0.0090	0.0230	0.0329
	500	0.0000	0.0045	0.0115	0.0165
	1000	0.0000	0.0022	0.0057	0.0082
Decay constant (m)	All	∞	15.02	1.84	1.29

⁴Measured for the mine water and slurry and from Telford et al. (1990) and Daniels (2004) for limestone.

⁵From Telford et al. (1990) and Daniels (2004).

The term ε_0 is the electrical permittivity of vacuum and all materials are nonmagnetic.

two-way time, or 25 m one-way distance at the limestone velocity, recorded at the eastern end of the line. This change in time is consistent with the triangular shape of the pillar and corresponding distance between the front, north wall and the back, south wall (Figure 1). After the BW reflection, a reflection can be observed at times and slope consistent with reflections from the far tunnel wall (FTW) of the southern tunnel (Figure 6), a distance of approximately 40 m. At the east end of the line, steep events have the correct times and slope for waves reflected from the east wall (EW) of the pillar and the far side of the eastern tunnel (Figure 6b). Strong events have the correct time and slope to be waves that are double reflected (DR) from the southern wall and then the eastern wall of the pillar, or vice versa (Figure 6).

Strong parallel reflections F1-F3 intersect the front wall of the pillar (zero time) at the locations of known fractures (Figure 6b) and are interpreted to be due to these parallel fractures. Although spatially semicontinuous, the amplitudes of these reflections are highly variable. An additional reflection with a different slope is observed

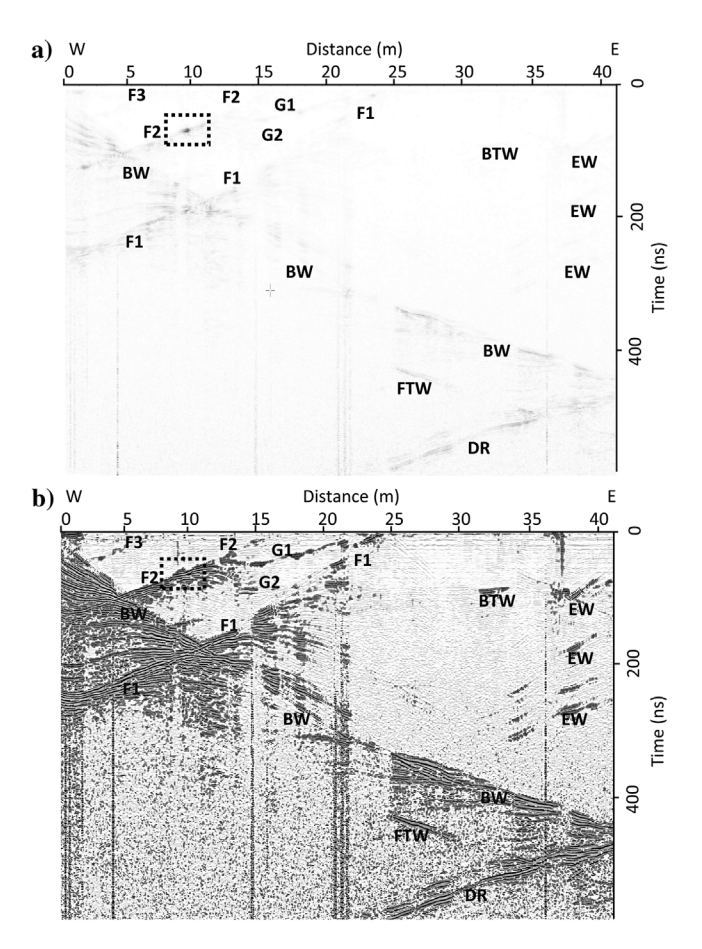


Figure 6. GPR 250 MHz unmigrated data after amplitude correction, plotted (a) at low gain to show strong reflections and (b) at high gain to show weaker reflections. Dashed box contains the maximum amplitude. BTW, air-wave reflection from the tunnel wall behind the operator; BW, reflection from the pillar's southern back wall; FTW, reflection from the far wall of the southern tunnel; EW, reflections from the pillar's east wall and the far wall of the eastern tunnel; DR, double reflection from the southern and eastern walls of the tunnel; F1-F3, reflections from a set of fractures exposed on the pillar's northern front wall; and G1 and G2, reflections interpreted to be another fracture set.

between F1 and F2, labeled G1 (Figure 6b). A short reflector G2 is parallel to G1 and at a later time.

AMPLITUDE CORRECTION

The reflection from the BW of the pillar enables relative and absolute amplitude calibration. To correct for nongeometric attenuation as a function of distance, the most common procedure is to observe many different reflections in a single trace, assume those reflections to be of equal average amplitude, and fit an exponential decay to their amplitude as a function of time (e.g., Claerbout, 1985). The radar data (Figure 6) have only a small number of reflections on any trace, so this method will not work. However, the observed reflection from the BW occurs at varying two-way time across the line and is a consistent limestone-air boundary, so attenuation was calibrated using this single reflection observed at different times on different traces. Amplitude calibration was then applied to Figure 6b prior to migration (Figure 7).

For each trace, the time and amplitude of the maximum negative peak (maximum absolute value) within a box centered on reflection BW (Figure 6) were picked prior to the spherical divergence correction. Pick amplitude on different traces was plotted as a function of pick time (Figure 8a). A best-fitting polynomial indicates a decay proportional to $t^{-1.6}$, which indicates attenuation faster than simple spherical divergence, which is t^{-1} in a constant-velocity rock. After spherical divergence correction (multiplying by t), the amplitudes decay less with time (Figure 8b). There is substantial variation in these amplitudes. The back, southern wall of the pillar is not flat at the scale of the approximately 47 cm wavelength (Table 1), especially at the cave and to the west (Figure 2). We interpret the amplitude variation to be primarily due to geometric constructive and destructive interference from waves reflected and scattered from a 3D rough surface, remembering that different times in Figure 8 correspond to different radar traces at different positions along the pillar's BW. In addition, amplitude variation can be caused by variable antennae coupling and orientation on the rough pillar wall. Because of this, the amplitude calibration should be considered to have large

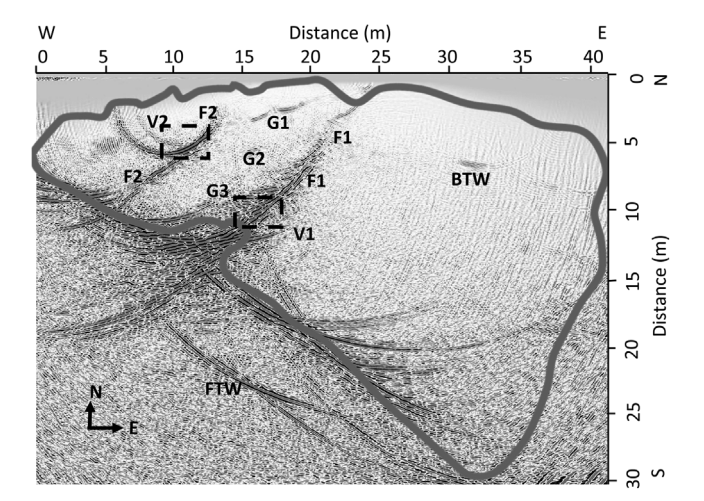


Figure 7. GPR 250 MHz depth-migrated image with the same interpretation as Figure 6. The gray outline is the surveyed pillar. F1 and F2, reflections from a parallel set of fractures exposed on the pillar's northern front wall; G1-G3, reflections interpreted to be a conjugate fracture set. V1 and V2 are interpreted as voids.

errors. These errors are estimated to be less than a factor of two based on trace-to-trace consistency, consistency between independently acquired lines in the 3D grid, and amplitudes of the known tunnel and cave reflections.

The best-fitting exponential decay constant for Figure 8b is 345 ns in two-way time or approximately 40 m in two-way distance traveled. This is larger than the 15 m decay constant estimated in Table 1 from the rock parameters. Neither number is precise, but both indicate that tens of meters of good signal penetration is to be expected. After correcting for this attenuation, the BW reflection amplitudes are more consistent as a function of the traveltime, which is proportional to the distance (Figure 8c). These spherical divergence and attenuation corrections were applied to the 2D and 3D data at all frequencies.

REFLECTION COEFFICIENTS

Real fractures observed on the pillar wall create strong reflections in the radar data (F1-F3 in Figure 6b). However, the observed distance between the fracture walls is mostly closed at the pillar wall, touching or dripping water but not visibly open except a few locations near the top, where gaps <1 cm are observed. The fracture can be considered as a thin layer with two reflecting boundaries: rock to fluid air or water and fluid back to the same rock. Traditionally, the wavepath-parallel resolution in reflection data is defined as the minimum distance between two boundaries that can be distinguished from one another. This thickness is the quarter-wavelength tuning thickness, where the maximum constructive interference occurs between signals reflected from the front walls and BWs of the thin layer (Yilmaz, 2001). If the layer is thicker than a quarter wave-

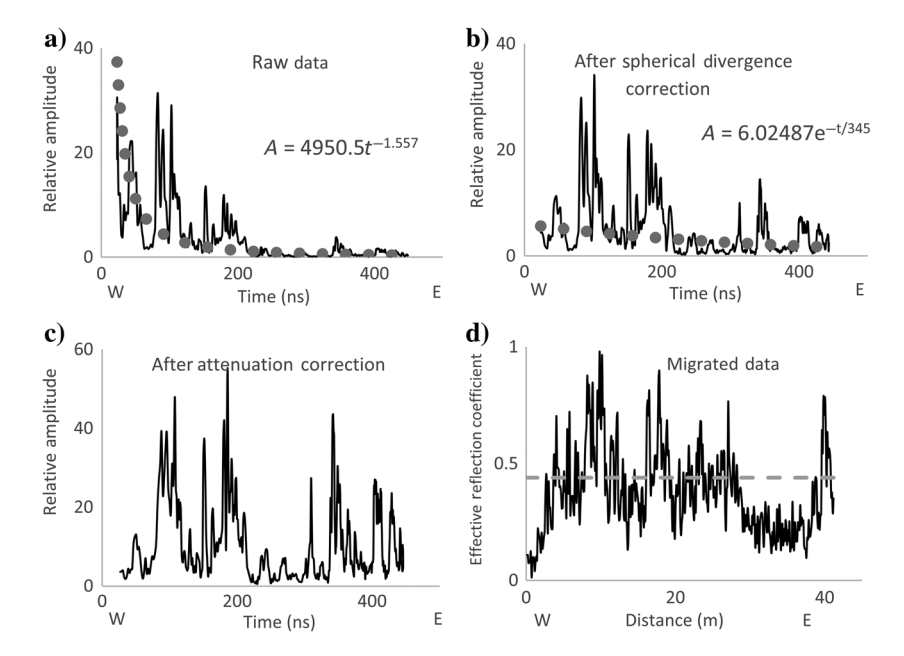


Figure 8. Maximum amplitude of the BW reflection from all traces in Figure 6, plotted versus the time of the reflection. (a) Amplitude prior to spherical divergence correction, and best-fitting power law (circles). (b) Amplitude after spherical divergence correction, and best-fitting exponential decay (circles). (c) Amplitude after attenuation correction. (d) Amplitude picked in a similar way from the BW reflection in the migrated data of Figure 7, plotted as a function of the west–east position. The amplitude axis in (d) was converted to a reflection coefficient by multiplying by a constant to match the average amplitude (the dashed line) to the limestone-air reflection coefficient of 0.44.

length at the velocity of the layer material, two separate reflections might be resolved. This requires the signal wavelet to be short and simple; the radar wavelet is approximately 3 cycles long (the right side of Figure 9a and 9c) and therefore not ideal. Layers thinner than a quarter wavelength result in rapid decay of the reflection amplitude and an effective wavelet that approaches the derivative of the original wavelet (the left side of Figure 9a and 9c) (Kalweit and Wood, 1982). The observed 250 MHz wavelet shown in Figure 9 has a dominant period corresponding to a frequency of approximately 290 MHz. At this frequency, a quarter wavelength in the fracture fluid is 26 cm in air or 3 cm in water (Table 2). However, much thinner observed fractures produced strong radar reflections in Figure 6b.

Synthetic radargrams were created using the convolutional model to simulate a thin fluid-filled fracture wedge (Widess, 1973; Hall, 2015). The radar wavelet was extracted from the data, and the velocities are from Table 2 (Figure 9). The fluid-rock velocity contrasts are very strong, resulting in a -0.56 reflection coefficient for a limestone-water boundary and +0.44 for limestone-air. For comparison, rock-rock or sediment-sediment reflection coefficients in GPR and seismic applications are typically much weaker at 0.01-0.1. Therefore, even though the reflection coefficient decreases rapidly for thin fractures, it remains stronger than typical radar reflections to a layer thickness of <1/40 wavelength (Figure 9). Therefore, very thin fractures, on the order of millimeters for water infill and centimeters for air infill, create reflections with amplitudes comparable with sediment-sediment or rock-rock boundaries (e.g., Kallweit and Wood, 1982; Lane et al., 2000; Kovin, 2011). Note that this is detecting the presence and location of the fracture, not resolving its two walls as separate reflectors. This ability to detect fractures

> with very thin apertures is further aided by low radar noise underground and by the lack of interfering stratigraphic reflections in the massive limestone.

MIGRATION

For non-1D structures, seismic or radar wavefield image processing called migration is required to convert the signal recorded as a function of time (Figure 6) to its true position in the subsurface (e.g., Grasmueck, 1996; Yilmaz, 2001). The topography on the data acquisition surface is usually corrected with static shifts in time and a corresponding movement of the stations vertically down to a flat surface. However, when the surface topography is rough or large compared with the wavelength, or when imaging near-surface or steeply dipping structures, these static shifts distort the wavefield and degrade image quality (e.g., Berryhill, 1979; Wiggins, 1984; Heincke et al., 2005). In these cases, topography should be included in the migration algorithm (e.g., Reshef, 1991; Gray and Marfurt, 1995; Lehmann and Green, 2000; Dujardin and Bano, 2013). Rock faces in general often have large roughness compared with radar wavelengths.

Two-dimensional or 3D Kirchhoff prestack depth migration (e.g., Wiggins, 1984; Lehmann

and Green, 2000; McClymont et al., 2008; Jin and Heuermann, 2012; Dujardin and Bano, 2013) was applied to all of the pillar radar data. The algorithm that was used can properly image steep features while directly incorporating the true station topography and preserving the amplitudes. The algorithm computes traveltimes using a finite-difference solution to the eikonal equation in a gridded velocity model.

The migration was performed using the limestone velocity of 0.117 m/ns and also using velocities ± 0.002 and ± 0.005 m/ns to confirm the optimum imaging velocity. Overlaying the known perimeter of the pillar on the migrated images confirms that the velocity measured with direct waves is also best for migration. The air velocity was not used in the tunnels during migration, so the far tunnel wall FTW reflection will be in the wrong location and slope. Similarly, air or water within fractures, voids, and the cave were not included in the velocity model. The 2D data were migrated in two dimensions, so any 3D geologic structure has the potential to harm the image. For the 3D data, the line spacing

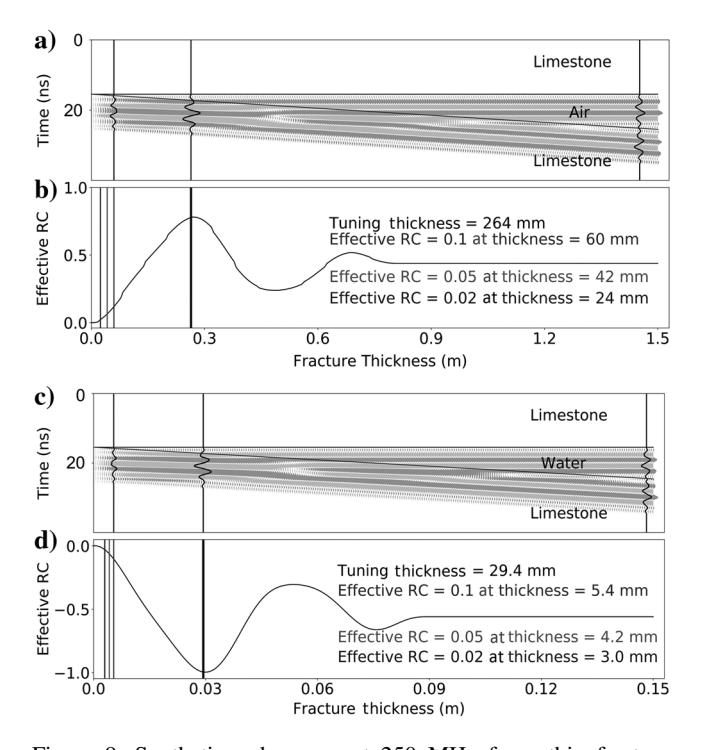


Figure 9. Synthetic radargrams at 250 MHz for a thin fracture wedge within limestone filled with (a) air and (c) water, using the wavespeeds in Table 1. The wavelet was extracted from the BW reflection in Figure 6. The wedge thickness is 10 times wider for the air wedge than for water, to compensate for the factor of nine difference in fluid wavespeeds. Wiggle traces show the source wavelet reflected from two boundaries at the right, the quarterwavelength wavelet with maximum constructive interference at the left-center, and approximately 1/20 wavelength destructive interference approximating the derivative of the wavelet at the left. Corresponding (b) air and (d) water wedge reflection amplitude, or effective reflection coefficient, versus wedge thickness. The quarter-wavelength (\(\mathcal{\psi} \)4) maximum-amplitude tuning thickness is indicated. The wedge thickness is also indicated for apparent reflection coefficients of 0.02, 0.05, and 0.1, corresponding to the three vertical lines at the left side of (b and d).

of 0.5 m was weakly aliased, producing circle-shaped anomalies that distract from but do not destroy the reflection image.

With the constant velocity, the migration preserves true amplitudes. However, the antenna radiation pattern, which emits a stronger signal perpendicular to the wall and a weaker signal parallel to the wall (e.g., Warren and Giannopoulos, 2017), was not included in the migration algorithm. This would have been difficult to accurately implement given the roughness and rapidly varying orientation of the pillar wall and antennae, but it was also not possible within the available migration algorithm. Therefore, amplitudes are approximately preserved for a given reflector slope, but steeper slopes should have stronger amplitudes than shown relative to flatter slopes. Like the amplitude analysis of Figure 8, this adds another approximation to the amplitude discussion below. We argue based on lateral consistency, however, that true amplitudes are preserved within a factor of less than 2.

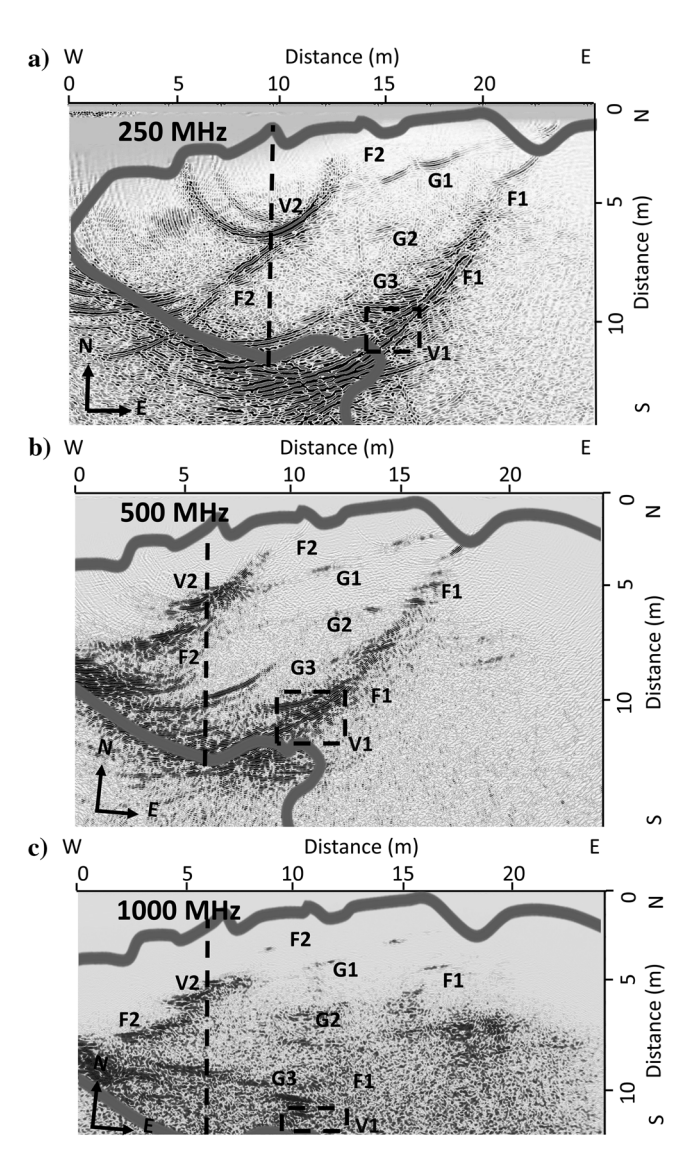


Figure 10. Migrated GPR images at (a) 250 MHz, (b) 500 MHz, and (c) 1000 MHz for the western half of the pillar, with an interpretation similar to Figure 7. The dashed black lines indicate the traces shown in Figure 11.

INTERPRETATION

The 2D radar data acquired in a horizontal line on the vertical pillar wall produce horizontal cross sections through the pillar. Radar reflections and scattering observed at 250, 500, and 1000 MHz (Figures 7 and 10) correlate spatially but differ in detail, which aids the geologic interpretation. The mine tunnels and pillar are entirely within the massive limestone ore formation with no internal stratigraphy. Therefore, reflections and aligned scattering within the pillar are interpreted as fractures and voids along fractures.

Geologic mapping of fractures within the mine and the 3D radar image (discussed later) indicate that the fractures are roughly vertical, so the horizontal 2D images closely represent a true structure rather than an out-of-plane structure. However, the exposed fractures, cave, and mined tunnel walls are not perfectly planar. These surfaces that act as reflectors include irregularities at the centimeter to meter scales, scales that are similar to the radar wavelength and radar footprint (the Fresnel zone) on a reflector (Table 2). In two dimensions, this can complicate the signature of the rough reflector into an imbricated pattern of overlapping reflections. In addition, signals scattered from 3D structures out of the plane of the image are not accounted for by 2D migration and can affect the continuity and quality of the migrated images.

The radar velocity contrast between the limestone pillar's far wall and air in the southern tunnel results in a very strong reflection amplitude (0.44 reflection coefficient, computed from Table 2). However, the pillar BW reflection (Figures 7 and 10) is not continuous everywhere and varies strongly in amplitude. These variations are interpreted to be due to irregular wall relief. The BW is most rugged in the cave and to the west, which is where the BW reflection is more scattered (Figures 7 and 10). The southeastern end of the BW is not imaged after migration (Figure 7) because no raypaths from the front wall intersect the eastern approximately 10 m of the BW at normal incidence, as required for the law of reflection.

Although reflections from the wall of the tunnel behind the radar operator are greatly reduced in the 250-1000 MHz data that were

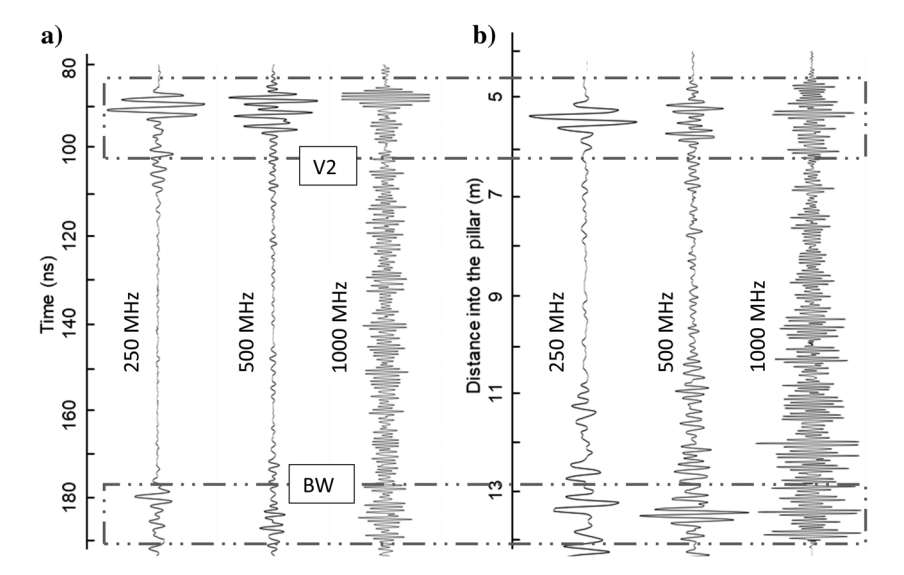


Figure 11. Radar traces through the V2 void at the location indicated in Figure 10. (a) Unmigrated radar data and (b) migrated image. Each trace was amplitude corrected along the trace, but the amplitudes cannot be compared between traces. BW, back wall; V2, void 2.

acquired with shielded antennae (Figure 5), an air-wave reflection is observed at irregular locations in the unmigrated and migrated images (BTW, Figures 6 and 7). This is due to a combination of the strength of the air-wave reflection from the tunnel wall, irregular gaps between the antennae and the rough pillar wall that allow energy to be reflected back from the front wall, and perhaps imperfect antenna shielding. The air-wave reflection is located in the migrated image (Figure 7) at a distance of approximately 5 m in the pillar, which is approximately 40% of the tunnel width because the air wave is migrated at the limestone rather than air velocity. Understanding the nature of potential air-wave artifacts is important when interpreting GPR data.

The eastern wall of the pillar and the east tunnel are roughly perpendicular to the radar line on the northern wall of the pillar (Figure 1). Reflections from the eastern walls are observed in the unmigrated data (EW, Figure 6b), but these reflections are for raypaths that travel roughly parallel to the pillar's front wall. Therefore, these reflections are migrated to the front corner of the pillar or, in the case of the east tunnel's far wall, beyond the image (Figure 7). Because migration only accounts for a single reflection, the double reflection from the back and east pillar walls (DR, Figure 6) is not migrated properly, but it fortunately migrates outside the image (Figure 7).

The reflection from the far wall of the southern tunnel (FTW, Figure 6) traveled through the entire pillar, was transmitted into the air in the tunnel, reflected, and returned back to the receiver. Approximately 40 m distance of the FTW reflector indicates that the 250 MHz radar could have imaged geologic features much further into limestone than the width of the pillar. The FTW reflector is imaged only approximately 5 m beyond the BW reflection (Figure 7), approximately 40% of the true tunnel width because the back-tunnel air wave was migrated at the limestone velocity. The southern tunnel's far wall runs the entire length of the pillar. However, only the section of it to the east of the cave is well imaged (FTW, Figure 7). This is interpreted to be because the pillar's BW is very rough from the cave to the western corner, scattering

> any energy transmitted into the tunnel. Analogous to seismic imaging beneath complex salt structures, the BW of the pillar and the air velocity needs to be accurately built into the migration velocity model to image the far tunnel wall past this rough surface (e.g., Yilmaz, 2001).

> Fractures F1-F3 are observed in the front tunnel where the radar data were acquired, and radar reflections from these fractures occur at the correct location at the front wall (Figures 7 and 10). In the nonmigrated data, reflections from fractures F1 and F2 cross reflections from the nonmigrated BW of the pillar (Figure 6b). Migration moves the reflections to their correct locations and to an orientation consistent with that observed in the mine tunnels (Figures 7 and 10). Migration is essential to place these steeply sloping features in their correct locations and orientations. Fractures F1-F3 are almost perpendicular to the BW of the pillar, so normal-incidence raypaths hitting the far ends of these fractures correspond to radar acquisition at the western corner of the tunnel, data that were

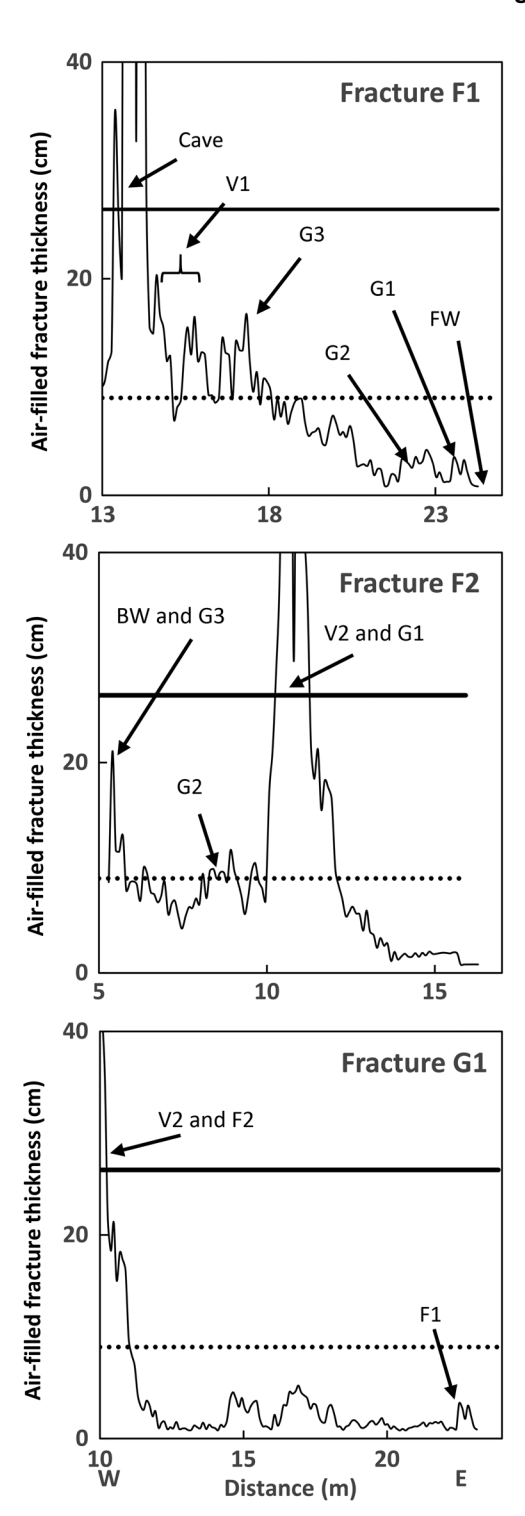


Figure 12. Aperture or thickness for fractures F1, F2, and G1 versus the west-east position. The aperture was computed from the 250 MHz radar reflection amplitude of Figure 10a using Figures 8d and 9b, assuming air-filled fractures. For water-filled fractures, the aperture is approximately 9 times thinner or, within error, the labeled units can be converted to millimeters. Feature labels are the same as Figure 7. The horizontal solid line is the thickness at $\lambda/4$ (maximum tuning). Above the dotted line, the fracture could be $>\lambda/4$, but this is considered unlikely. Geometric effects on amplitudes are not considered, so these plots are more indicative than quantitatively accurate.

not acquired. This results in some curved migration artifacts that extend beyond the BW reflection (Figures 7 and 10). The 500 and 1000 MHz lines did not extend as far to the west; therefore, the curved migration artifacts are shallower, partly within the pillar.

The migrated radar images confirm that F1 at the front wall of the pillar connects to the cave in the BW and that F2 extends from the front to the BW where it is rough and fractured (Figure 10). The F1 reflection has amplitudes near the cave that are comparable with the BW reflection. These large amplitudes are interpreted to be due to an open void V1 that is an extension of the cave that cannot be observed from the southern tunnel (Figures 7 and 10). F1 weakens toward the front wall where the fracture walls are mostly in contact (closed). The F2 reflection is also weak at the front wall, where the fracture is closed but has a very large amplitude in the middle of the pillar at location V2 (Figures 6, 7, and 10). Fracture F3 is closed on the front wall and has a smaller amplitude in the unmigrated image (Figure 6b). F3 is difficult to discern in the migrated images, at least in part due to large-amplitude artifacts associated with V2 (Figure 10).

Additional reflections in the radar images, G1-G3, are semiparallel to each other between F1 and F2 (Figure 10). No fractures are observed in the pillar walls with this orientation. These reflections are interpreted to be caused by a second fracture set. G3 has a more complex geometry. Where it is close to F1, it is parallel to G1 and G2, but further west it changes direction to become parallel to the northwestern wall of the cave (Figures 7 and 10).

The large amplitude reflector or scatterer where G1 intersects fracture F2 (at V2, Figures 6, 7, and 10) is interpreted to be an open void in the rock. Very large amplitudes are observed on multiple radar traces in the 2D unmigrated data (Figure 6a), on parallel lines in the 3D data, and in the 200 MHz data acquired with different equipment, so these large amplitudes are interpreted to be caused by a real geologic feature. V2 has very strong amplitude at 250 MHz and is relatively localized in the unmigrated data, but does not have a noticeable diffraction hyperbola (Figure 6). The very strong amplitude indicates quarter-wavelength tuning. However, the length of V2 is smaller than a wavelength, and it should behave like a point diffractor. A thin-layer reflector is highly dependent upon the angle of incidence; at different angles, the raypaths within the layer are shorter or longer. For point-diffractor raypaths in one direction, the noncircular void V2 thickness is interpreted to be ideally tuned to create very strong amplitudes. In other directions, V2 is too thick or thin to create strong scattering; therefore, the point diffractor hyperbola is much weaker. Geometric constructive interference in two or three dimensions may contribute to the strong amplitudes.

Because migration assumes uniform scattering, the very large localized unmigrated amplitude of V2 and weak hyperbola result in a circular migration artifact that is poorly cancelled (Figures 7 and 10a); this is the classic migration impulse response. Tests at extreme migration velocities all produce this result, confirming that it is not caused by an overmigration velocity error. Although the migration artifact could be reduced by artificially clipping the large premigration amplitude, this would modify the geometry, amplitude, and interpretation of fracture F2 and void V2, the primary targets of this work.

The interpreted void V2 has a much larger amplitude in the unmigrated data and the migrated image at 250 MHz than at either 500 or 1000 MHz (Figures 6, 7, 10, and 11). The amplitude of the V2 reflection or scattering at 250 MHz is about twice the BW amplitude (Figure 11), and the BW is a very strong reflection between limestone and air (reflection coefficient 0.44). Assuming the V2 void is

filled with air, this would indicate a maximum tuning effect at a quarter wavelength, which is a void of approximately 26 cm wide (Figure 9b). If V2 contains water, which produces a limestone-water reflection coefficient of 0.54, then the void is only approximately 3 cm wide (Figure 9d) due to the much slower radar velocity (Table 2). Determining the polarity of the reflections, and thus distinguishing water from air, is difficult due to the approximately three cycle long radar wavelet (Figure 9a and 9c). The V2 reflection is large, but it is a little smaller than the BW reflection, at 500 MHz (Figure 11), consistent with the void being about a wavelength wide at the higher frequency (Figure 9). The reflection character is also

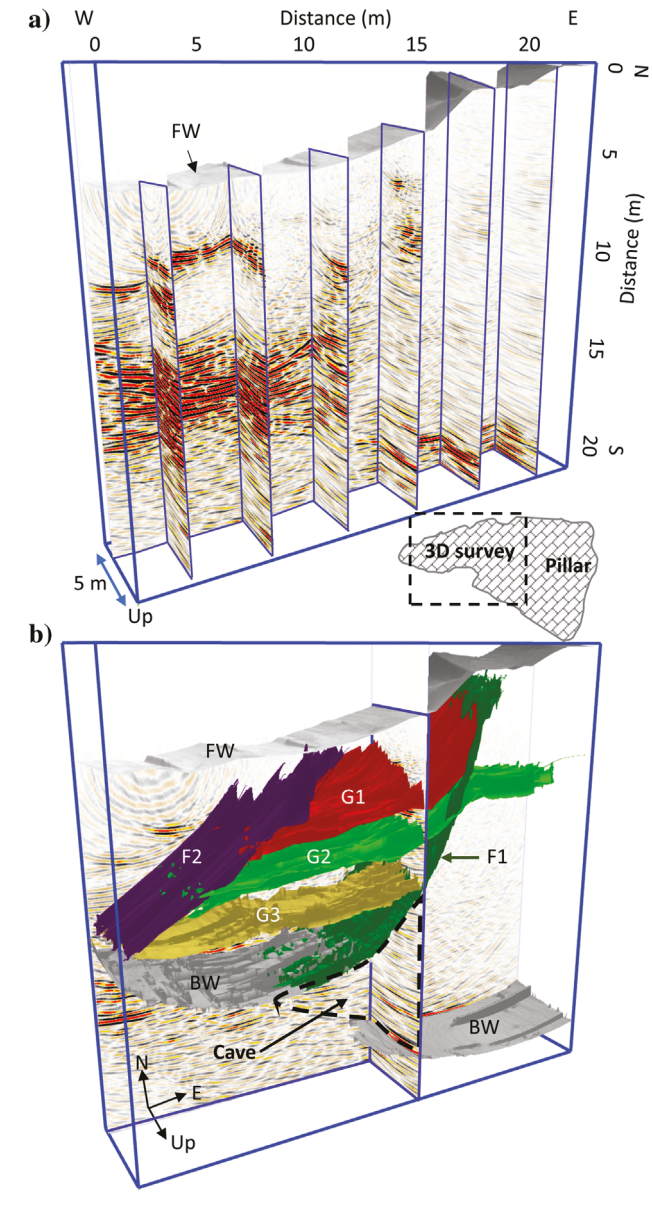


Figure 13. Oblique view from above of the 3D migrated radar volume. The volume is within the western half of the pillar (the inset map) from 0.5 to 5.5 m above the tunnel floor. (a) Radar images on a horizontal slice near the bottom of the volume and several vertical north-south slices. (b) Manually picked reflection surfaces from fractures and the pillar walls. The gray surfaces represent the front walls and BWs of the pillar. The labels are the same as in Figure 7.

more complex at 500 and 1000 MHz, consistent with a feature or features larger than the shorter wavelengths at these frequencies.

In the nonmigrated 250 MHz data, the fractures appear to be semicontinuous (Figure 6b), but the migration image suggests a less continuous structure (Figure 10a). The higher frequency migrated images (Figure 10b and 10c) also suggest a more discontinuous structure. The variable amplitudes and character of each fracture along its surface are interpreted to be caused by some combination of laterally variable fracture aperture; geometric offsets, bends, or curvature; multiple interfering fractures; different fluids filling the fractures; and 3D artifacts in 2D data. However, part of the image differences at different frequencies is due to the difficulty of acquiring high-frequency data on a rough pillar wall. Steeply sloping F1-2 reflections at 500 and 1000 MHz appear as a discontinuous set of events that are nonparallel to the fracture or disappear entirely (Figure 10b and 10c), a common artifact caused by spatial aliasing. Although the station spacing was not aliased (Table 1), bridging of the wall roughness caused by data acquisition on a wooden plank created time delays that were a significant fraction of the dominant period. This damaged coherency of the wavefields, particularly for steeply sloping reflectors, and it could not be corrected by simple static time shifts in the air. However, the spatial consistency of the variation along the fractures at different frequencies, especially for shallowly sloping G1 and G2, indicates that first-order variability along the fractures is real and geologic.

The amplitudes of the fracture reflections are assumed to represent the fracture aperture to interpret trends. The true amplitude processing and the average amplitude from the BW reflection were used to calibrate amplitude to the reflection coefficient (Figure 8d). Apparent reflection coefficients from thin layers of less than a quarter wavelength (the left side of Figure 9b and 9d) were then used to convert the observed fracture reflection amplitudes in Figure 10a to the fracture aperture (Figure 12). Because the effects of the fracture geometry and other errors in amplitude discussed above are ignored,

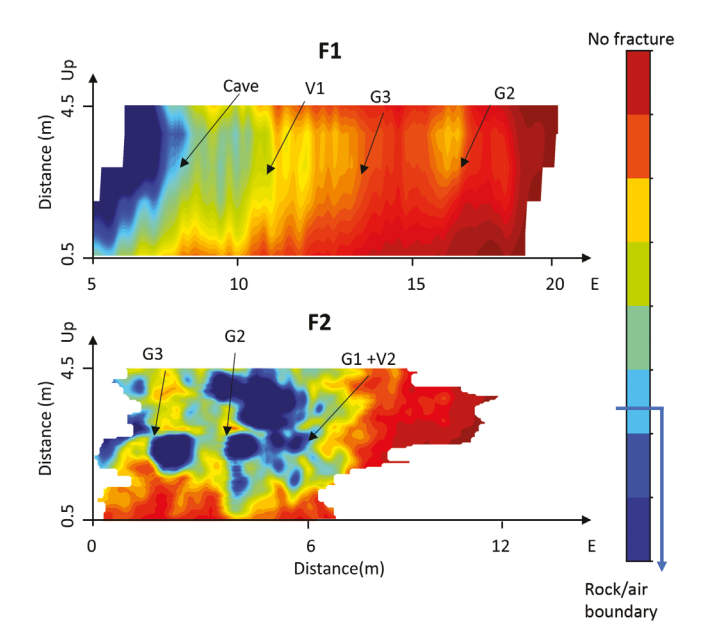


Figure 14. Map of the radar reflection amplitude on fracture surfaces F1 and F2 from the 3D migrated radar image (Figure 13). The reflection amplitude is interpreted to represent the fracture aperture. The labels are the same as in Figure 7.

these values should be considered indicative of trends and magnitude within a factor of approximately 2, not the absolute aperture. Assuming that the fractures are air filled, they are centimeters thick. If water filled, the fractures are millimeters thick. For wider fractures and voids, it seems more likely that mine pumping has drained the water. However, narrower fractures or isolated voids may remain water-filled. The fractures leak water every time it rains, so the fluid may change temporally; the data were acquired during dry weather.

Fracture F1 decreases gradually from an open cave toward the BW of the pillar to a couple of centimeters of air (millimeters of water) near the front wall (Figure 12). In detail, however, the local variation along the fracture is as much as a factor of two. Fracture F2 behaves similarly, closing gradually from open (approximately 10 cm of air or approximately 1 cm of water) near the BW to an order of magnitude thinner near the front wall (Figure 12). However, F2 is interrupted by a very large amplitude, which is interpreted as an open void (V2). Fracture G1, in comparison, has two larger amplitude spots with apertures of a few centimeters (millimeters if water) but is otherwise mostly closed, except where it intersects F2 at V2 (Figure 12).

The migrated 3D volume provides valuable additional insight into the fracture networks in the pillar (Figure 13). The 2D images (Figures 7 and 10) correspond to a horizontal section approximately 1 m from the bottom of the 3D volume (Figure 13). The vertical dimension of 3D data acquisition is only approximately 3 m, and the migrated grid 5 m, but it is sufficient to verify that all of the fractures are subvertical. The amplitude of fracture F1 gets stronger moving upward within the pillar (Figures 13 and 14), interpreted as a widening trend of the fracture. This is consistent with the observed narrow fracture in the front, the northern tunnel and the large cave in the back, and the southern tunnel, both of which widen upward. Fractures F2 (Figures 13 and 14), G1, G2, and G3 (Figure 13) also increase in amplitude upward, but they are not as large in amplitude and therefore are not as open. Other reflectivity between the labeled fractures also increases upward, suggesting more pervasive fracturing. The interpreted void V2s amplitude remains large but increases in spatial size upward (Figure 14).

At every single intersection of fractures G1, G2, and G3 with fractures F1 and F2, the reflection amplitude increases relative to nearby on either fracture (Figures 10, 12, and 14). These amplitudes are particularly enhanced and strong along F2, including void V2 (Figures 10, 12, and 14). These larger amplitudes are interpreted as fractures that are more open or as voids. These fracture-intersection features also become more open upward in the pillar.

The F and G fracture sets are each a parallel or subparallel set with roughly the same spacing between fractures (Figures 10 and 13). The angle between fracture sets F and G is consistent with conjugate fractures with a horizontal maximum stress that is oriented "northeast" in the local coordinate system. In an absolute orientation, this maximum compression direction is consistent with the modern continental stress (Zoback and Zoback, 1980).

The fracture sets display a ladder pattern with a set of longer F fractures, and the conjugate set of G fractures that are relatively short and terminate at the long fractures (Figures 10 and 13). This geometry is consistent with the radar reflection amplitudes and with hazards encountered in the mine, both of which indicate that the F fracture set dominates and is more open. The 2D and 3D migrated radar images show consistently larger amplitudes at the intersections of fracture sets F and G (Figures 10, 12, and 14). This indicates a larger aperture, and in some cases voids, along the intersections of fractures. Fracture set F is much more important than G for the mechanical strength and fluid flow within the mine. However, the radar data indicate that the dominant groundwater flow paths and dissolution of the limestone occur at the intersections of the G fractures with the F fractures. Therefore, fracture set G, while less dominant than F, helps control the location of maximum groundwater flow and the formation of the karst system.

DISCUSSION

Rock-penetrating radar successfully detected and located known features of the mine pillar: subparallel fractures exposed on the wall where the radar data were acquired, a mine tunnel meters to tens of meters away, and a natural karst cave (Figures 6, 7, 10, and 13). Radar imaged the continuation of known fractures inside the pillar from the front to the back of the pillar. In addition, the radar detected and located a previously unknown set of subparallel fractures (G1-G3) and a larger void (V2) within the pillar (Figures 6, 7, 10, and 13).

Reflectors were detected within the rock at distances of > 25 m using 250 MHz radar, approximately 15 m at 500 MHz, and approximately 10 m at 1000 MHz (Figures 6, 7, and 10). The 250 MHz antenna was ultimately chosen for the 3D survey for having shielded antenna, reducing data acquisition effort, and most importantly being able to image features deep enough for the miners to plan for mitigating hazards.

Fractures with aperture or opening much smaller than the wavelength of the radar are detected. Due to the strong dielectric contrast between limestone (like most minerals) and either air or water, fracture apertures less than a 50th of a wavelength produced clear reflections (Figures 6, 7, 9, 10, and 12). For 250 MHz radar, the detectable aperture is at the millimeter scale for water-filled fractures and centimeter scale for air-filled fractures; these apertures scale inversely with radar frequency. Thinner fractures could probably have been imaged if the pillar front wall was smoother.

Migration is essential to properly locate radar reflectors that are not subparallel to the data acquisition surface, in this case, the pillar's front wall. The local roughness of the pillar wall is at scales of centimeters to meters, comparable with the radar wavelength; the pillar-scale curvature of the front wall is many wavelengths; and reflectors exist at large angles (>55°) relative to the front wall. Standard static topography corrections are insufficient to correct for these factors, necessitating the use of a less common migration algorithm that migrates from the true topography. Despite the use of LIDAR surveying, the roughness of the rock wall and the radar antenna bridging this roughness degraded the images of steeper structures at the higher radar frequencies used (Figure 10b and 10c).

Postmigration, radar imaged two sets of subparallel and subvertical fractures (Figures 10 and 13). The F fractures are mapped to their known true orientation, including connecting F1 at the front wall to the cave in the far tunnel. The G fracture set is mapped to an orientation that is consistent with a conjugate fracture set. The F fracture set is associated with mine control (structural collapse) and flood hazards in the mine, and it has strong radar reflection amplitudes. Fracture set G is of lesser importance to mine hazards, was not previously known in the pillar, and has weaker radar reflection amplitudes.

After calibrating radar attenuation using reflections from the far tunnel wall, the fracture aperture was mapped along each fracture (Figures 12 and 14). Each fracture changes in aperture over distances of meters, presumably due to minor fracture structures such as offsets and kinks. In addition to the newly discovered void V2 at the intersection of the F2 and G1 fractures, larger reflection amplitude is observed at every intersection of the F and G fractures. The fractures and voids indicate that opening, and therefore permeability and karst dissolution, is generally larger for fracture set F, but is largest where two conjugate fractures intersect.

The goal of this study was to enable the mine to detect and characterize fractures prior to excavation. In less than an hour of data acquisition and with simple data scaling, the goal of detection was achieved in the field, producing plots similar to Figure 6. Radar detected thin-aperture fractures at distances into the rock much further than a normal blast in this mine (approximately 5 m). One caution is that the fracture orientation must enable detection from existing tunnels while obeying the law of reflection: The radar receiver must be able to "see" the radar transmitter in the fracture as if the fracture were a mirror.

Numerical modeling of rock mass strength for ground control or permeability for fluid flow requires additional fracture characterization. Accurate fracture location, geometry, aperture, and perhaps fracture fluid (water versus air) requires careful centimeter-scale position surveying and migration processing from true topography. With some software development, this could be achieved in two dimensions within a day or two of acquiring the data. Full 3D imaging requires days of fieldwork and weeks of analysis; however, 2D imaging may meet routine mining operational needs.

CONCLUSION

Consistent with previous studies that used radar to detect fractures behind a rock face, this study demonstrates that radar is well suited for fracture detection in electrically nonconductive rock. In this study, the radar detected known fractures and voids, and it also discovered additional, previously unknown fractures and voids. Fractures with apertures as small as a 50th of the radar wavelength were detected to a depth of > 50 wavelengths. Depending on the target fracture distance and aperture, up to several tens of meters distance, an appropriate radar frequency can be chosen. Simple detection may be sufficient for some applications, but migration is required to accurately locate and orient fractures that are not parallel to the data acquisition surface. In many mining environments, the roughness of the rock surface and/or fractures at modest or larger angles to that surface necessitate that the surface "topography" be included in the migration algorithm. Migration imaging in two and three dimensions successfully imaged a fracture network within a pillar and calibrated this to known features exposed in the mine. Reflection amplitudes can be calibrated to a known reflector, such as an adjacent tunnel, to determine the aperture of thin fractures. The fracture apertures and geometry mapped in this study enabled an improved understanding of the relationship between two fracture sets, one of which was not previously known. In this mine, one fracture set is more open and the primary hazard to mining. However, water flow, dissolution, and subsequent opening is strongest at the intersection of fractures, so mapping the second fracture set can help determine where the first set may be most hazardous. Geometry and aperture are invaluable parameters for mining engineers to perform numerical modeling of ground control to avoid collapse or to model fluid flow. GPR imaging of fractures and voids enables mine personnel to characterize these features ahead of the mining face prior to drilling, blasting, and excavation. Detection prior to operations could reduce safety and operational risks by allowing a change to the mining scheme, sequence, or implementation of ground control and grouting techniques ahead of excavation.

ACKNOWLEDGMENTS

This work was conducted within and received partial funding to J. A. Hole from the Center for Advanced Subsurface Earth Resource Models (CASERM), which received funding from industry sponsors and the National Science Foundation's Industry-University Cooperative Research Centers program. Funding was also provided by NIOSH to NP for this work. A. Abbasi Baghbadorani received scholarship support from SEG. Lhoist North America and its employees are thanked for the mine access, logistical support, and professional knowledge. S. Holbrook allowed us to use his GPR equipment and provided advice. M. Lemon provided technical assistance. Sensors & Software Inc. (EKKO_Project), Halliburton (SeisSpace Promax), and DownUnder GeoSolutions (DUG Insight) provided software and technical support for this work.

DATA AND MATERIALS AVAILABILITY

Data associated with this research can be obtained by contacting the corresponding author and upon agreement from the mine operator/owner.

REFERENCES

- Annan, A. P., J. L. Davis, and D. Gendzwill, 1988, Radar sounding in potash mines, Saskatchewan, Canada: Geophysics, 53, 1556-1564, doi: 10.1190/
- Apel, D. B., and V. Dezelic, 2005a, Using ground penetrating radar (GPR) in analyzing structural composition of mine roof: Mining Engineering, 57,
- Apel, D. B., and V. Dezelic, 2005b, Evaluation of high frequency ground penetrating radar (GPR) in mapping strata of dolomite and limestone rocks for ripping technique: International Journal of Surface Mining, Reclamation and Environment, **19**, 260–275, doi: 10.1080/13895260500275418.
- Arosio, D., 2016, Rock fracture characterization with GPR by means of deterministic deconvolution: Journal of Applied Geophysics, 126, 27-34, doi: 10.1016/j.jappgeo.2016.01.006.
 Baek, S.-H., S.-S. Kim, J.-S. Kwon, and E. S. Um, 2017, Ground penetrating
- radar for fracture mapping in underground hazardous waste disposal sites: A case study from an underground research tunnel, South Korea: Journal
- of Applied Geophysics, 141, 24–33, doi: 10.1016/j.jappgeo.2017.03.017. Baggett, J., A. Abbasi, J. Monsalve, R. Bishop, N. Ripepi, and J. A. Hole, 2020, Ground-penetrating radar for karst detection in underground stone mines: Mining, Metallurgy, and Exploration, 37, 153-165, doi: 10.1007/
- Berryhill, J. R., 1979, Wave-equation datuming: Geophysics, 44, 1329-1344, doi: 10.1190/1.1441010
- Bliss, J. D., T. S. Hayes, and G. J. Orris, 2008, Limestone A crucial and versatile industrial mineral commodity, USGS Fact Sheet 2008–3089, https://pubs.usgs.gov/fs/2008/3089/fs2008-3089.pdf, accessed 1 October 2020.
- Centers for Disease Control and Prevention (CDC), 2019a, Mining topic: Ground control overview, https://www.cdc.gov/niosh/mining/topics/ GroundControlOverview.html, accessed 2 October 2020.
- Centers for Disease Control and Prevention (CDC), 2019b, Mining topic: Geologic characterization, https://www.cdc.gov/niosh/mining/topics/ GeologicCharacterization.html, accessed 2 October 2020.
- Christie, M., G. P. Tsoflias, D. F. Stockli, and R. Black, 2009, Assessing fault displacement and off-fault deformation in an extensional tectonic setting using 3-D ground-penetrating radar imaging: Journal of Applied Geophysics, **68**, 9–16, doi: 10.1016/j.jappgeo.2008.10.013. Claerbout, J. F., 1985, Imaging the earth's interior: Blackwell Scientific Pub-
- lications.
- Daniels, D. J., 2004, Ground penetrating radar, 2nd ed.: Institution of Engineering and Technology, https://app.knovel.com/hotlink/toc/id:

- kpGPRE0007/ground-penetrating-radar-2/ground-penetrating-radar-2, accessed 4 June 2021.
- Deparis, J., and S. Garambois, 2009, On the use of dispersive APVO GPR curves for thin-bed properties estimation: Theory and application to fracture characterization: Geophysics, **74**, no. 1, J1–J12, doi: 10.1190/1
- Dérobert, X., and O. Abraham, 2000, GPR and seismic imaging in a gypsum quarry: Journal of Applied Geophysics, **45**, 157–169, doi: 10.1016/S0926-9851(00)00025-2.
- DownUnder GeoSolutions, 2020, DUG insight (Version 4.7): DownUnder GeoSolutions, http://www.dug.com, accessed 4 June 2021.
- Dreybrodt, W., 1988, Processes in karst systems: Physics, chemistry, and
- geology: Springer, Series in Physical Environment 4. Dujardin, J.-R., and M. Bano, 2013, Topographic migration of GPR data: Examples from Chad and Mongolia: Comptes Rendus -
- 345, 73–80, doi: 10.1016/j.crte.2013.01.003. Grandjean, G., and J. C. Gourry, 1996, GPR data processing for 3D fracture mapping in a Marble Quarry (Thassos, Greece): Journal of Applied Geophysics, 36, 19-30, doi: 10.1016/S0926-9851(96)00029-
- Grasmueck, M., 1996, 3-D ground-penetrating radar applied to fracture imaging in gneiss: Geophysics, 61, 1050–1064, doi: 10.1190/1.1444026. Grasmueck, M., R. Weger, and H. Horstmeyer, 2004, Three-dimensional
- ground-penetrating radar imaging of sedimentary structures, fractures, and archaeological features at submeter resolution: Geology, 32, 933,
- Gray, S. H., and K. J. Marfurt, 1995, Migration from topography: Improving the near-surface image: Canadian Journal of Exploration Geophysics, 31,
- Grégoire, C., and F. Hollender, 2004, Discontinuity characterization by the inversion of the spectral content of ground penetrating radar (GPR) reflections — Application of the Jonscher model: Geophysics, 69, 1414–1424, doi: 10.119 00/1.1836816.
- Grodner, M., 2001, Delineation of rockburst fractures with ground penetrating radar in the Witwatersrand Basin, South Africa: International Journal of Rock Mechanics and Mining Sciences, 38, 885-891, doi: 10.1016/
- Gross, R., A. Green, H. Horstmeyer, K. Holliger, and J. Baldwin, 2003, 3-D georadar images of an active fault: Efficient data acquisition, processing and interpretation strategies: Subsurface sensing technologies and applications: An International Journal, **4**, 19–40, doi: 10.1023/A: 1023059329899.
- Hall, M., 2015, tuning_wedge_V2.py, Agile_Geoscience, https://github.com/seg/tutorials-2014/blob/master/1412_Tuning_and_AVO/tuning_prestack_v2.py, accessed 4 June 2021.
 Halliburton, 2020, SeisSpace® ProMAX® (Version 5000.10.0): Hallibur-
- Heincke, B., A. G. Green, N. J. van derKruk, and H. Horstmeyer, 2005, Acquisition and processing strategies for 3-D georadar surveying a region characterized by rugged topography: Geophysics, 70, no. 6, K53-K61, doi: 10.1190/1.21224
- Jeannin, M., S. Garambois, C. Grégoire, and D. Jongmans, 2006, Multiconfiguration GPR measurements for geometric fracture characterization in limestone cliffs (Alps): Geophysics, **71**, no. 3, B85–B92, doi: 10.1190/1
- Jin, S., and P. Heuermann, 2012, Prestack depth migration from topography in foothills using a hybrid reverse-time migration: European Association of Geoscientists and Engineers, Conference Proceedings, First EAGE/ Asociación Colombiana de Geólogos y Geofísicos del Petróleo Latin American Geophysics Workshop, cp-278-00014, doi: 10.3997/2214-
- Johnson, R. B., and J. V. DeGraff, 1988, Principles of engineering geology: Wiley.
- Jol, H. M., 2009, Ground penetrating radar theory and applications: Elsevier, https://app.knovel.com/web/toc.v/cid:kpGPRTA00F/viewerType:toc//root_slug:ground-penetrating-radar?kpromoter=marc, accessed 4 June
- Kallweit, R. S., and L. C. Wood, 1982, The limits of resolution of zero-phase wavelets: Geophysics, 47, 1035–1046, doi: 10.1190/1.1441367.
- Kovin, O., 2011, Mapping of evaporite deformation in a potash mine using ground penetrating radar: Upper Kama Deposit, Russia: Journal of Applied Geophysics, **74**, 131–141, doi: 10.1016/j.jappgeo.2011.04.009. Lane, J. W., M. L. Buursink, F. P. Haeni, and R. J. Versteeg, 2000, Evalu-
- ation of ground-penetrating radar to detect free-phase hydrocarbons in fractured rocks Results of numerical modeling and physical experiments: Groundwater, 38, 929–938, doi: 10.1111/j.1745-6584.2000
- Lehmann, F., and A. G. Green, 2000, Topographic migration of georadar data: Implications for acquisition and processing: Geophysics, **65**, 836–848, doi: 10.1190/1.1444781.
- Leucci, G., R. Persico, and F. Soldovieri. 2007, Detection of fractures from GPR data: The case history of the Cathedral of Otranto: Journal of

- Geophysics and Engineering, 4, 452-461, doi: 10.1088/1742-2132/4/4/
- Li, S., S. Li, Q. Zhang, Y. Xue, B. Liu, M. Su, Z. Wang, and S. Wang, 2010, Predicting geological hazards during tunnel construction: Journal of Rock Mechanics and Geotechnical Engineering, **2**, 232–242, doi: 10.3724/SP.J 2010.00
- Liu, H., Z. Shi, J. Li, C. Liu, X. Meng, Y. Du, and J. Chen, 2021, Detection of road cavities in urban cities by 3D ground-penetrating radar: Geophysics, **86**, no. 3, WB25–WB33, doi: 10.1190/geo2020-0384.1.
- Liu, W., J. Rostami, and E. Keller, 2017, Application of new void detection algorithm for analysis of feed pressure and rotation pressure of roof bolters: International Journal of Mining Science and Technology, 27, 77-81, doi: 10.1016/j.ijmst.2016.11.009.
- Longoni, L., D. Arosio, M. Scaioni, M. Papini, L. Zanzi, R. Roncella, and D. Brambilla, 2012, Surface and subsurface non-invasive investigations to improve the characterization of a fractured rock mass: Journal of Geophysics and Engineering, **9**, 461–472, doi: 10.1088/1742-2132/9/5/461. Markovaara-Koivisto, M., T. Hokkanen, and E. Huuskonen-Snicker, 2014,
- The effect of fracture aperture and filling material on GPR signal: Bulletin of Engineering Geology and the Environment, 73, 815–823, doi: 10.1007/
- McClymont, A. F., A. G. Green, R. Streich, H. Horstmeyer, J. Tronicke, D. C. Nobes, J. Pettinga, J. Campbell, and R. Langridge, 2008, Visualization of active faults using geometric attributes of 3D GPR data: An example from the Alpine Fault Zone, New Zealand: Geophysics, 73, no. 2, B11-B23, doi: 10.1190/1.2825408
- Orlando, L., 2003, Semiquantitative evaluation of massive rock quality using ground penetrating radar: Journal of Applied Geophysics, **52**, 1–9, doi: 10.1016/S0926-9851(02)00229-X.
- Pipan, M., E. Forte, F. Guangyou, and I. Finetti, 2003, High resolution GPR imaging and joint characterization in limestone: Near Surface Geophysics, 1, 39–55, doi: 10.3997/1873-0604.2002006.
- Porsani, J. L., W. A. Sauck, and A. O. S. Júnior, 2006, GPR for mapping fractures and as a guide for the extraction of ornamental granite from a quarry: A case study from Southern Brazil: Journal of Applied Geophysics, **58**, 177–187, doi: 10.1016/j.jappgeo.2005.05.010.

 Prego, F. J., M. Solla, X. Núñez-Nieto, and P. Arias, 2016, Assessing the
- applicability of ground-penetrating radar to quality control in tunneling construction: Journal of Construction Engineering and Management, 142, 06015006, doi: 10.1061/(ASCE)CO.1943-7862.0001095. Qi, Y., T.-C. J. Yeh, Y. Wu, M. Li, and Y. Hao, 2017, Comparing control
- methods of water inrush disaster using mathematical programming: Mod-elling, analysis and a case study: Geomatics, Natural Hazards & Risk, 8,
- Reshef, M., 1991, Depth migration from irregular surfaces with depth extrapolation methods: Geophysics, **56**, 119–122, doi: 10.1190/1
- Sensors and Software, 2018, EKKO_Project (Version 5): Sensors & Software Inc.
- Stevens, K. M., G. S. Lodha, A. L. Holloway, and N. M. Soonawala, 1995, The application of ground penetrating radar for mapping fractures in plutonic rocks within the Whiteshell Research Area, Pinawa, Manitoba, Canada: Journal of Applied Geophysics, 33, 125-141, doi: 10.1016/0926-
- Telford, W. M., L. P. Geldart, and R. E. Sheriff, 1990, Applied geophysics, 2nd ed.: Cambridge University Press.
- Theune, U., D. Rokosh, M. D. Sacchi, and D. R. Schmitt, 2006, Mapping fractures with GPR: A case study from Turtle Mountain: Geophysics, 71, no. 5, B139–B150, doi: 10.1190/1.2335515.
- Toshioka, T., T. Tsuchida, and K. Sasahara, 1995, Application of GPR to detecting and mapping cracks in rock slopes: Journal of Applied Geophysics, 33, 119–124, doi: 10.1016/0926-9851(95)90035-7.
- Warren, C., and A. Giannopoulos, 2017, Characterization of a ground penetrating radar antenna in lossless homogeneous and lossy heterogeneous environments: Signal Processing, **132**, 221–226, doi: 10.1016/j.sigpro 2016.04.010.
- Widess, M. B., 1973, How thin is a thin bed?: Geophysics, 38, 1176-1180,
- doi: 10.1190/1.1440403. Wiggins, J. W., 1984, Kirchhoff integral extrapolation and migration of non-planar data: Geophysics, 49, 1239–1248, doi: 10.1190/1.1441752. Yilmaz, Ö., 2001, Seismic data analysis: SEG.
- Young, R. A., Z. Deng, K. J. Marfurt, and S. E. Nissen, 1997, 3-D dip filtering and coherence applied to GPR data: A study: The Leading Edge, 16, 921–928, doi: 10.1190/1.1437699
- Zoback, M. D., and M. L. Zoback, 1980, State of stress in the conterminous United States: Journal of Geophysical Research, Solid Earth, **85**, 6113–6156, doi: 10.1029/JB085iB11p06113.

Biographies and photographs of the authors are not available.